Materials Chemistry and Physics 294 (2023) 126929

Contents lists available at ScienceDirect

Materials Chemistry and Physics

journal homepage: www.elsevier.com/locate/matchemphys

Periodic DFT computation of rotational barriers for linear molecules in zeolites: Validation *via* zero-point energies and isotopic heat difference values of adsorbed H_2/D_2

A.A. Rybakov [a], D.N. Trubnikov [a], D.P. Vercauteren [b,**], A.V. Larin [a,*]

[a] Department of Chemistry, Moscow State University, GSP-2, Leninskie Gory, Moscow, 119992, Russia
[b] Namur Institute of Structured Matter, Laboratory of Computational Physico-Chemistry, University of Namur, Rue de Bruxelles 61, Namur, B-5000, Belgium

HIGHLIGHTS

- Agreement with experimental differences of heats of adsorption of D_2 and H_2 is shown.
- Method to calculate the barriers for H_2/D_2 rotation in MeY is given with cNEB + VASP.
- Al distribution in NaY windows is confirmed basing on GGA and hybrid DFT schemes.
- Quadrupole defines rotational barrier of 8 gases near Me = Na and Ca cations in MeY.
- CO, NO, N_2O dipoles have poor influence on rotational barrier near divalent cation.

GRAPHICAL ABSTRACT

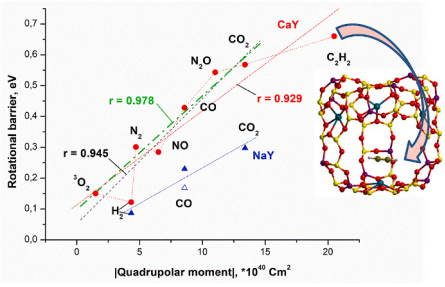

ABSTRACT

A climbing image nudged elastic band (cNEB) algorithm was applied on the basis of density functional theory (DFT) calculations of the rotational barriers of eight linear molecules (H_2, N_2, O_2, CO, CO_2, NO, N_2O, C_2H_2) adsorbed in NaY and NaCaY periodic zeolite models at the MeII cation sites (the Na or Ca metal cation in the SII site) located near the 6R windows. A specific approach is applied for molecules with positive quadrupole (H_2, C_2H_2) and small negative quadrupole ($^3O_2$) moments while applying cNEB. The obtained T-geometry relative to the cation is the most frequent case for H_2 adsorption in cationic form sieves and metalorganic frameworks (MOFs). The computed barriers for the T- and other linear (L) orientations are in good correlation with the quadrupole moments taken from literature irrespective of the dipole values (CO, NO, N_2O). In the case of NaY, the Al distribution per 6R sites is also discussed which allowed finding particular favorite adsorption sites. The calculated zero-point energies relative to the obtained rotational barriers regarding the H_2 - D_2 pair result in a qualitative agreement with the experimental isotopic difference in the H_2/D_2 adsorption heats in NaY which ultimately lead to the H_2/D_2 separation coefficient.

1. Introduction

Mono– and divalent metal cations are often the main source of the presence of an electric field at the surface and inside adsorbents. This leads to observe forbidden IR bands for linear molecules without dipole. The well-known absence of rotational branches of the vibrational transitions for adsorbed diatomic molecules (CO_2 [1], N_2 [2–4], CO [4–10], O_2 [3,11,12], H_2, D_2 [3,13], HD [13]), for example in zeolites, confirms that the rotational motions are suppressed while the rotational sub-bands observed in MOFs allowed more detailed analyses of the

* Corresponding author.
** Corresponding author.
E-mail addresses: daniel.vercauteren@unamur.be (D.P. Vercauteren), larin@phys.chem.msu.ru (A.V. Larin).

https://doi.org/10.1016/j.matchemphys.2022.126929
Received 16 May 2022; Received in revised form 3 October 2022; Accepted 15 October 2022
Available online 29 October 2022

rotational potentials [14–16] as well as inelastic neutron scattering data [17–20]. In this domain, we showed that even in presence of monovalent cations (Na), the rotation of CO near the NaII cation (the Na located in the SII site) in NaY zeolite is more hindered compared to the relatively easier non-rotational diffusion between the NaII cations [21]. CO possesses a small dipole so that the origin of the rotational hindrance might be questioned. A relevant discussion was also held many years ago by Kington and MacLeod who showed the dominant role of the molecular quadrupole moment in the decrease of the differential adsorption heat with coverage (from 0.01 to 0.3) for H_2, N_2, O_2, CO, and CO_2 in natural chabazite (NaCa-chabazite) and calcium chabazite (Ca-chabazite) zeolites [22]. Intuitively, one supposes a loss of the favored molecular orientation relative to the electric field vector at high coverage (already at the coverage of 0.3 and higher [22]) due to interactions with other adsorbed species. It means that a molecular re-orientation takes place within the same coverage interval (<0.3) so that the rotational barrier should also be directly related to the dipole and/or quadrupole values. In this respect, an attempt to connect the quadrupole moment and diffusion of N_2 and CO_2 in the Na-**ZSM**-5 forms at high Si/Al ratio (more than 20) was undertaken in terms of the molecular residence times at the cationic site [23]. Different models of gas separation in narrow pore zeolites [24–26] indeed emphasize the importance of the interaction between the molecular rotation of the adsorbate and the motions of the cation when passing the 8R windows (or double D8R) blocked by the cation.

An accurate description of molecular rotations in the adsorbed state is also of prime validity for the modeling of H_2/D_2 isotope separation in zeolites [27–29] and MOFs [30–35]. To determine either the kinetic or the static origin in the H_2/D_2 separation in flexible MOFs [32,33,35], adsorption energies of H_2 and D_2 should be precisely estimated because their difference is an important factor for their separation as well as regarding their difference between their zero-point energies (ZPE). The rotational energy fraction is an essential part of the total ZPE similarly to the ones from the intra-molecular vibration and of the center-of-mass (COM) modes. At a non-zero barrier, the rotational ZPE for ortho- and para-H_2 (para- and ortho- D_2) increases relative to $2B_{X2}$ and 0 (X = H or D), respectively, for a free X_2 rotor, $2B_{X2}$ being the rotational constant. Therefore, an accurate determination of the barrier is important for the calculation of the total H_2 or D_2 adsorption energy, for which the sum of vibrational and rotational ZPE values can take from 23 [31] to 43% [28] of the total adsorption energy.

The most predictable approach to evaluate the rotational barrier is to generate a series of "rotated" geometries for any linear molecule (X_2 or XY) located in the Me^{n+}-X_2 plane (Me = metal) between two stable Me^{n+}-X-X′ and Me^{n+}-X′-X minima. However, the application of such strategy to homonuclear molecules requires considering the possible variation of the cation – center-of-mass distance during rotation. The case of heteronuclear molecules is then more complex due to the parallel varying X–Y length for opposite orientations (for CO example, see values in Figs. 1 and 2 of ref. [21]), their variation being stronger than for homonuclear ones. As a result, even in the Henry's law region (without adsorbed nearest neighbors and respective interactions), one should consider more complex motions than described by a pure rotation due to its interaction with the other translational degrees of freedom. These translational-rotational interactions also contribute to the barrier profile so that the heat of adsorption changes with coverage as described in the work of Kington and MacLeod by 1959 [22]. Additionally, both molecular multipoles and polarizabilities will also vary upon physisorption in strong electrostatic fields. Numerical [36] and analytical [37] approaches to involve such corrections were shown, for example, for the H_2 case.

The difficulties described above for both homo- and heteronuclear adsorbates indicate that elaborate methods are required for assessing the respective "rotational" trajectory in the framework. In the present work aiming to evaluate the accuracy of the barrier - quadrupole correlation, we used the climbing image nudged elastic band (cNEB) code developed by Henkelman et al. [38,39] within VASP [40,41] to compute the rotational barriers for a set of diatomic (H_2, N_2, O_2, CO, NO) and linear polyatomic (CO_2, N_2O, C_2H_2) molecules including three of them with a small dipole moment (CO, NO, N_2O). The optimization of the adsorbate trajectory with cNEB permitted to include new distorted model geometry at each new rotation angle along the trajectory. The rotational barriers were calculated nearby the mono- and divalent cations in NaY and NaCaY (denoted as CaY below) zeolites and compared *versus* their quadrupole moments Θ (½Θ_{zz}) known from literature. The considered cationic sites at the 6R windows are the most frequent in the popular zeolite frameworks as the MeII type in **FAU** [42] or the MeI type in **LTA** [43]).

In Part 2, one presents the selected parameters for the calculations with the respective codes. Then, one depicts the geometries of the models optimized with VASP which are further considered as input for the cNEB method (Part 3.1). In Part 3.2, one describes all barriers obtained with cNEB and illustrates the relevance of the approach for MOFs by comparing the isosteric heat differences between H_2 and D_2 measured in zeolites and MOFs. The importance of the Al distribution in NaY is presented in Part 3.3 regarding particular types of NaII/6R sites. The calculation of the ZPE values and heat differences between H_2 and D_2 is presented in Part 3.4. An emphasized attention to the solution of the rotational problem for H_2 and D_2 is commented in Part 3.5. The importance of the anharmonic character of the potential energy (Part 3.6) and the relation between quantum and kinetic sieving effects in NaY (Part 3.7) for H_2/D_2 are shortly discussed. In the final part, one justifies the use of the cNEB analysis (Part 3.8), as well as additional possibilities to classify the specific cation-molecule interactions (Part 3.9).

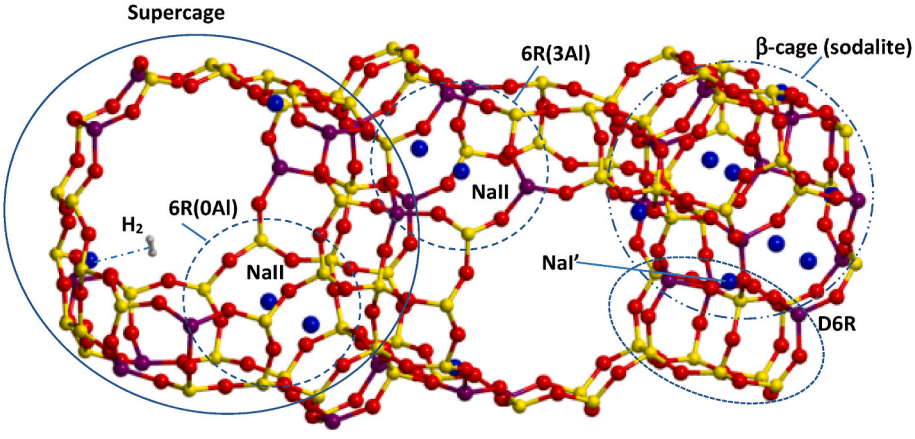

Fig. 1. General view of 2 supercages (one is shown by circle in solid line) and sodalite cage (dot-dot-dashed line) connected with double 6R (or D6R, dotted line), and two types of 6R(nAl) rings (dashed line) of NaY. The positions of NaI′ and NaII cations and H_2 molecule near the 6R(0Al) ring are depicted. Atom colors are gray (small spheres), red, blue, magenta, and yellow for H, O, Na, Al, and Si, respectively. (For interpretation of the references to color in this figure legend, the reader is referred to the Web version of this article.)

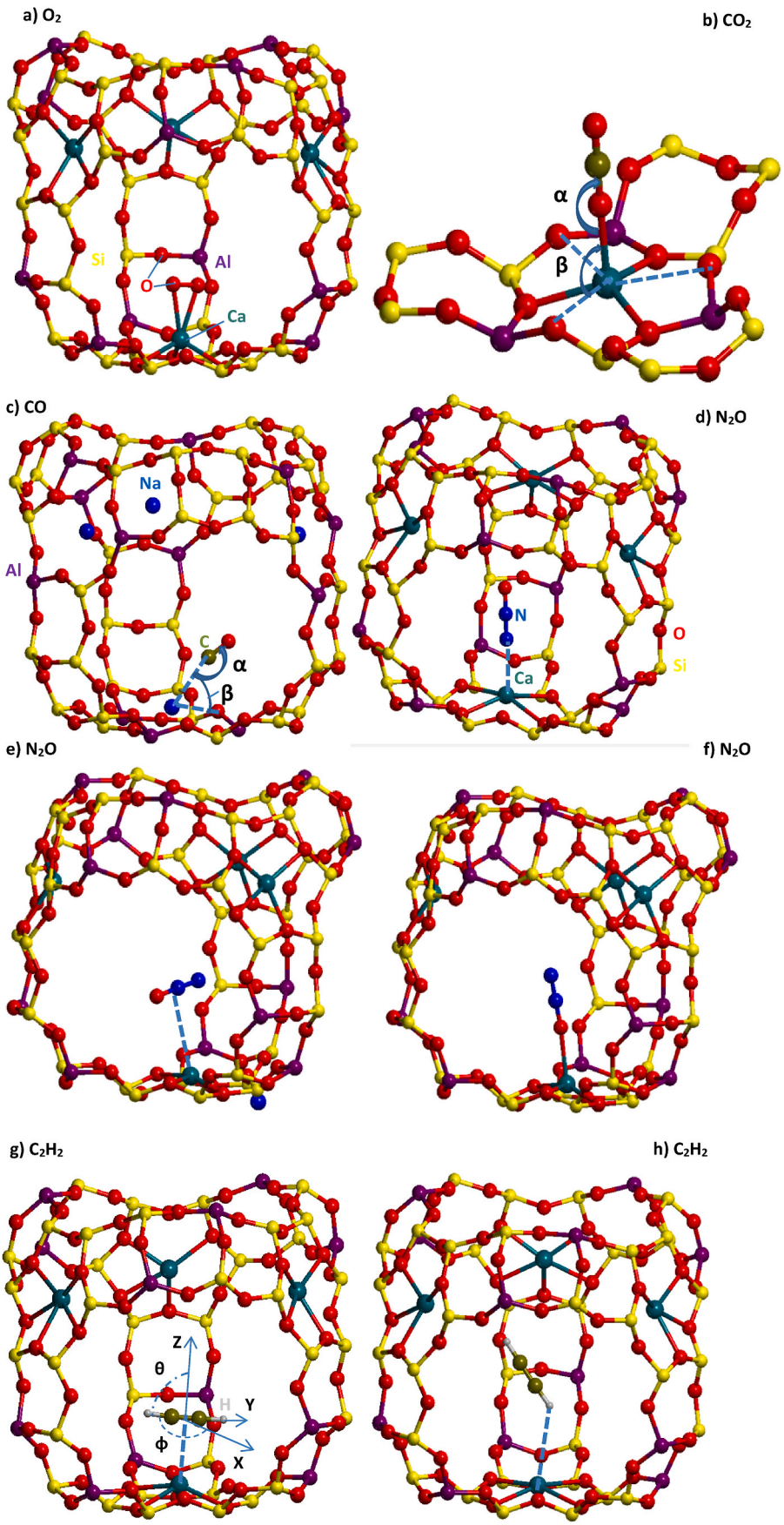

Fig. 2. Geometry of (a) O_2, (b) CO_2, (c) CO, (d–f) N_2O, and (g–h) C_2H_2 at the (a, b, d-h) CaII or (c) NaII sites of the MeY supercage (only one supercage is shown) for the case without Al atoms (a, d-h), with three Al atoms per 6R ring (b, c), at the (a-d, g) initial, (e, h) transition, and (f) final state of the molecular rotation. Angles (α, β) of the molecular axis deviations are shown in (b, c). Atom colors are gray (small spheres), olive, blue (two linked atoms), red, blue, magenta, yellow, cyan and green for H, C, N, O, Na, Al, Si, and Ca, respectively, in (c, d, g). (For interpretation of the references to color in this figure legend, the reader is referred to the Web version of this article.)

2. Computational details

Conventional models of MeY zeolite (Si/Al = 3) with the $Na_{12}Al_{12}Si_{36}O_{96}$ and $Na_4Ca_4Al_{12}Si_{36}O_{96}$ formula (denoted below as NaY, CaY) were built according to ref. [44]. For illustration, a fragment of NaY including 2 supercages and the sodalite cage connected with two double 6R rings (only one of two D6R rings is visible) is given in Fig. 1. The initial model with *F23* spatial group symmetry contains two supercages per unit cell and involves four 6R(3Al) rings with 3 Al atoms ($n_{Al} = 3$) and four 6R(0Al) rings without Al atoms ($n_{Al} = 0$). The supercage with four 6R(0Al) rings is shown in Fig. 1 by a solid circle, while the second supercage with four 6R(3Al) ring is in the center.

Plane wave computations with periodic boundary conditions using the PBE [45] and PBEsol [46] functionals were performed within the projector augmented wave (PAW) method [41,47] implemented in VASP [40,41]. Dispersive energy corrections were considered at the zero damping D3 [48,49] levels. Comparable accuracy of D3 corrections for periodic systems relative to that of D4 was shown in ref. [50]. Atomic charge density distributions were analyzed using the Bader [51], Mulliken [52] and Löwdin [53] schemes developed in the Bader [54] and Lobster [55] codes. The scripts provided by the Transition State Tools for VASP were used to build the initial images for the climbing image nudged elastic band (cNEB) calculations [38,39]. The energy cut-off was set to 500 eV. The Brillouin zone *k*-sampling was restricted to the Γ–point for the geometry optimization, the transition state (TS) search and the lowest energy path construction *via* the cNEB calculations, and the vibrational analyses. Regarding the application of denser *k*-grids for analogous zeolite cells [56], a 2 × 2 × 2 grid was also tested (Part 3.2) confirming that the use of the Γ–point for MeY is totally sufficient as, for example, shown in Ref. [57]. Vibrational frequencies were computed using the finite difference method (0.015 Å atomic displacements) as implemented in VASP. A spin-polarized solution was considered only for the ground triplet state of $^3O_2$ molecule.

As a test for the validation of the results obtained at the general gradient approximation (GGA) level of computations, the relative stabilities of the NaY periodic models with different Al distributions were also evaluated with the hybrid Hartree-Fock (HF)-DFT functional using CRYSTAL17 [58]. A middle-range corrected Henderson-Izmaylov-Scuseria-Savin (HISS) functional [59,60] was applied with the same atomic basis sets as recommended in CRYSTAL17 [58]: 8-511G for Na [61], TZVP for H [62], and 8-411G* for O, 88-21G* for Si, 85-11G* for Al [58] as for the GGA calculations. The basis sets for O, Al, and Si have already been tested earlier [63].

The LEVEL code was used to solve the 1D radial equation according to the Numerov-Cooley method for the H_2 (or D_2) center-of-mass vibration relative to the NaII cation [64]. Calculated points were approximated by 4th-order polynomials producing an equidistant grid (around 70–80 points) as input for LEVEL. The contributions to the ZPE values from two the other (translational) degrees of freedom for H_2 (or D_2) center-of-mass motions parallel to the 6R plane were evaluated as minor ones based on the hindered rotations for a "center--of-mass-zeolite" pseudo-diatomic molecule model in the center of the α-cage of the **LTA** zeolite [28,29]. 2D rotational models with the Sams-MacRury approach [65] were considered in an own home-made code that was already tested earlier for different van der Waals clusters [66] and Linde A type zeolites [28,29]. The figures of the 3D structure of the different models were drawn with MOLDRAW 2.0 [67]. Molecular motions along with the rotational trajectories (see SM) were obtained using wxMacMolPlt [68].

In order to apply the obtained V barriers for the calculation of the heat of H_2 adsorption in NaY, we adopted an H_2 model without coupling between the rotational and center-of-mass motions. Such approximation was successfully used both in zeolites [28,29] and MOFs [31,33]. The independent solutions for the center-of-mass vibration relative to NaII were obtained using the Numerov-Cooley method implemented in the LEVEL code [64]. A 2D rotational model was then developed using the Sams-MacRury approach [65]:

$$U = V \times Cos^2(\theta) + V_1 \times (1\text{-}Cos(n\varphi)) \quad (1)$$

wherein *n* is an integer value, θ, the angle between the "NaII(or CaII) → center-of-mass" vector and the adsorbate axis (Fig. 2g), and φ, the angle between the OX axis of the local coordinate system at the X_2 center-of-mass (X = H, D) and the adsorbate axis (Fig. 2g). The solution of the eigen-problem with the potential (Eq. (1)) was obtained with our own home-made code that was already tested for different molecular C_6H_6 – XY clusters with n = 6 [66] and Linde A type zeolites with n = 2 [28,29].

To outline, one should clearly separate the applications of three main codes used herein. VASP is the main work tool at the DFT GGA level for all the data. The accuracy of the relative stabilities of the NaY models at the DFT GGA has been verified with the hybrid DFT (HISS) functional using CRYSTAL. Single point computations with the hybrid DFT functionals like PBE0 are much more time consuming with VASP. The LEVEL code is only limited to the 1D radial equation using the anharmonic GGA potential energy obtained with the VASP code (the latter gives harmonic frequencies).

3. Results

3.1. Optimized geometry of the adsorbate molecular locations

Two main issues were considered. The first one is related to the analysis of the "quadrupole moment - rotational barrier" ratio for a series of different linear molecules mainly at the CaII site of the NaCaY form with the highest electric field and possibly the highest electric field gradient (few points were also calculated at the NaII sites of NaY for comparison). The emphasis on CaII was determined by the highest electrostatic value due to the highest Ca^{2+} atomic charge to reveal the possible correlation.

Regarding the quadrupole moment - rotational barrier ratio for the eight molecular gases, the CaII site model in CaY was selected without Al in the 6R ring ($n_{Al} = 0$) for which we estimated the Ca contacts only with the Si–O–Si oxygens of the 6R ring (Fig. 2). Such Ca coordination with the O atoms was found to be weaker compared to the other models with Al, therefore leading to the highest electrostatic field effect and gradient on the rotation. The relative stability of the optimized T-type (when the vector from the Me cation to the molecular center-of-mass is perpendicular to the molecular axis, Fig. 2g) agrees with the positive (H_2, C_2H_2) quadrupole moment. Linear (L) positions (Me located along the molecular axis, Fig. 2b, d, f) of the adsorbates relative to the Me cation correspond to negative quadrupole moments in the case of N_2, CO, NO, N_2O, CO_2. For O_2, its small negative quadrupole moment (Table 1) does not lead to the favored L-orientation because a larger dispersive energy is obtained for the T-type in the Me–O_2 orientation (Fig. 2a). The 2.711–2.742 Å range values calculated herein for CaY are in good agreement with the measured XRD experimental value 2.74 Å for Ca–C (O) in Ca-chabazite [69].

3.2. cNEB results regarding the "rotational barrier - quadrupole" correlation

To apprehend the rotational barrier - quadrupole correlation, one performed cNEB calculations for all eight adsorbates, H_2, N_2, O_2, CO, CO_2, NO, N_2O, and C_2H_2 in CaY, and for three of them, H_2, CO, and CO_2 in NaY located at the MeII sites with the various numbers of Al atoms (n_{Al}) in the nearest 6R ring. The initial and final configurations of the rotational trajectory were obtained for symmetric molecules *via* a permutation of two atoms of the same chemical element in the unique optimized position. For non-symmetric molecules, both the initial and final configurations were optimized.

For the molecules with a positive quadrupole, H_2 and C_2H_2, and for triplet $^3O_2$, a problem was noted while applying the cNEB scheme due to

Table 1
Literature sources regarding the experimental or calculated Θ quadrupole moments ($\times 10^{40}$ Cm^2, refs. in middle column) of the considered molecular species (dipoles are known for CO ($\mu = 0.0481$ ea$_0$) [70], NO ($\mu = 0.0622$ ea$_0$) [71], N_2O ($\mu = 0.0633$ ea$_0$) [72]) *versus* the rotational barriers V (eV) calculated in MeY ($n_{Al} = 0$) at the PBE/PAW level (Fig. 3).

Gas	Θ	Ref.	Me	V
O_2	−1.50	[89]	Ca	0.150
H_2	4.34	[90]	Ca	0.143[a)]
			Na	0.087[b)]
N_2	−4.72	[91]	Ca	0.301
			Ca[c)]	0.277
NO	−6.51	[92]	Ca	0.283
CO	−8.58	[91]	Ca	0.428, 0.486[d)] 0.457[e)]
			Na	0.235, 0.168[e)] 0.232[d)]
N_2O	−11.0	[93]	Ca	0.543
CO_2	−13.4	[91]	Ca	0.568, 0.575[c)]
			Na	0.298
C_2H_2	20.5	[94]	Ca	0.660

[a)] 0.124 eV from the assignment of H_2/CaI spectra in Na_4Ca_4A with similar CaII sites at 6R rings [73]; 0.173 eV from empirical pair wise potentials [28].
[b)] 0.084 eV for H_2/NaI in Na_4Ca_4A and 0.083 eV for H_2/NaI in $Na_{12}A$ from empirical pair wise potentials [28].
[c)] PBEsol-D2.
[d)] PBEsol-D3BJ.
[e)] $n_{Al} = 3$ (open triangle in Fig. 3).

the obtained T-geometry with the cation at equilibrium (Fig. 2a, g). As a result, cNEB led to a more preferable path *via* a φ-rotation (in the plane perpendicular to the vector passing through the cation and molecular center-of-mass) compared to the path of θ-rotation (in the plane passing through the cation and molecular axis, Fig. 2g) having larger barrier. Therefore, additional steps were developed to evaluate the barrier of θ-rotation with cNEB. A combination of the two initial profiles with one common intermediate state (similar to the probable TS) taken as the initial geometry for cNEB allowed to get the profile along the θ-rotation and thus to obtain the transition state (with imaginary frequency) and the rotational barrier V.

The calculated rotational barriers *versus* the quadrupole moments are shown in Fig. 3. No correspondence between the molecular sizes and barriers is observed, since the vdW radii of N_2 is larger than the one of CO, this in opposite ratio with their barriers. For the widest set of eight molecules, one observes a good correlation irrespective of the small dipole values for CO ($\mu = 0.0481$ ea$_0$) [70], NO ($\mu = 0.0622$ ea$_0$) [71] and N_2O ($\mu = 0.0633$ ea$_0$) [72]. The correlation even improves from 0.929 to 0.978 while discarding the data for the molecules with positive quadrupoles (H_2 and C_2H_2[1]). The final coefficient of 0.929 for all 8 molecules is satisfactory.

The calculated rotational V barrier value of 0.143 eV for H_2 (Table 1) is in a reasonable agreement with the known experimental value of 0.124 eV at the similar CaI site in NaCaA [73]. Using empirical schemes, an overestimated barrier of 0.173 eV was previously obtained for the H_2 barrier above CaI in NaCaA (Table 7 in ref. [28]), while a better agreement between the computed barrier of 0.084 eV at NaI in NaCaA [28] is noted with the current 0.087 eV value (Table 1). The good correlation with the empirical estimations of the H_2 barrier [28] justifies the comparisons with the other evaluations from empirical schemes in MOFs [18,19]. It is worthwhile to note that the barriers above Na^+ obtained herein are comparable with the ones estimated for other cations in MOF, 0.086 eV above Y^{3+} in Y-FTZB [18], 0.076 eV above Mg^{2+} in $[Mg_3(O_2CH)_6)]$ [19], due to a denser cationic coordination by the ligands in MOFs than in zeolites. This idea is in agreement with the observation of the rotational structure of vibrational transitions in MOFs [14–16] which is depressed in the cationic form zeolites due to higher electric field/field gradient and hence of the rotational barriers.

[1] One should note the accurate computational quadrupole value for H_2 [90] and experimental one for C_2H_2 [94]. When considering the experimental quadrupole for NO, -4.62×10^{-40} Cm^2, *versus* the recommended theoretical value 6.51×10^{-40} Cm^2 [92], the correlation slightly improves (Fig. 3).

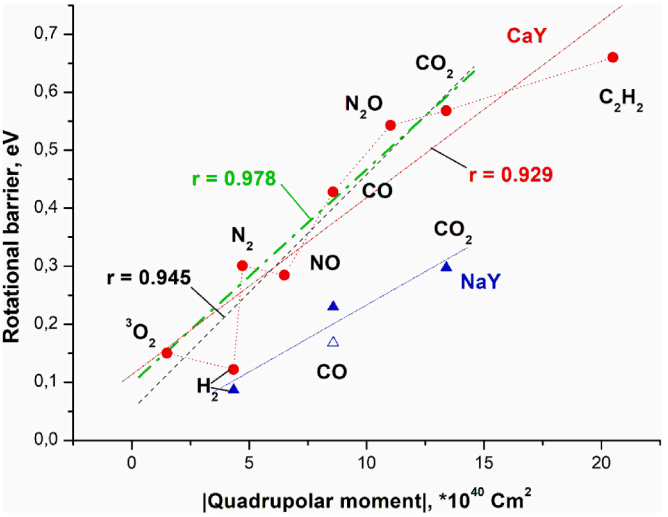

Fig. 3. Rotational barriers (eV) of H_2, O_2, NO, CO, CO_2, N_2O, CO_2, and C_2H_2 in CaY (circles in red connected by dotted line) or NaY (triangles in blue) zeolites for the case without Al atoms (filled symbols) and with three Al atoms per 6R ring (open symbol) *versus* the absolute values of the molecular quadrupoles ($\times 10^{40}$ Cm^2). Correlation coefficients are given for all 8 molecules (dot-dashed line in red; correlation of 0.928), without C_2H_2 (linear fit for 7 points *via* dashed line in black; correlation of 0.945), without H_2 and C_2H_2 (linear fit for 6 points *via* dot-dashed thick line in green; correlation of 0.978). For NaY, a line fitted through 3 points for the case without Al atoms per 6R is also given. (For interpretation of the references to color in this figure legend, the reader is referred to the Web version of this article.)

Regarding the small H_2 barrier of 0.087 eV in NaY (Table 1), some test using a wider $2 \times 2 \times 2$ k-grid instead of one Γ-point was realized at two (H_2) and one (N_2, CO_2) points of symmetric molecules along their rotation trajectories and at the minima for two orientations of non-symmetric molecules CO, NO, and N_2O in CaY and NaY (H_2 only) as calculated earlier using the Γ-point. The respective changes (Table S1) with the denser grid are less than 2×10^{-3} eV for the total energy at both points and for the heat of adsorption, and even less than 10^{-3} eV for the rotational barrier of H_2 (as difference of the energy values). This smallness of the energy variations at the $2 \times 2 \times 2$ k-grid relative to those calculated at the Γ–point only confirms that considering the latter is sufficient for all gases.

The good correlation for the widest "Θ - V" series of values for CaY (Fig. 3) means that the barrier value is mainly determined by an electrostatic term proportional to the interaction E_{elec} energy between the molecular quadrupole and field gradient:

$$E_{elec} \approx -\Theta \times q_i \times (3\cos^2(\theta_i) - 1)/(4R_i^3) \quad (2)$$

wherein Θ is $(1/2)\Theta_{zz}$, θ_i, the angle between the electrostatic field vector and molecular axis (that should be close to $\pi - \alpha$, rad, Fig. 2c), and R_i, the distance between the atomic charge q_i and the molecular center-of-mass. The use of Θ gas state properties for the molecules in (Eq. (2)) is justified by the small charge transfer (Table 2). Due to the proportionality between q_i (Table 3) and E_{elec} *via* Eq. (2), the ratio between the nearest atomic charge and the rotational barrier V is proportional to E_{elec}. The obtained double difference between the CO rotational barriers over NaII (in NaY) and CaII (in NaCaY) sites is in agreement with the predicted difference from the three applied electron partition schemes (Bader, Mulliken, Löwdin) for $n_{Al} = 0$ or 1 (Table 4). It allowed to show that the rotational barriers increase by a factor of two when switching from Na to

Table 2
Charge transfer (Bader (B), Mulliken (M), Löwdin (L)) from the CO molecule towards the CaII and NaII cations in CaY and NaY, respectively, with different number of Al atoms per 6R ring (n_{Al}), calculated with the Bader [54] and Lobster [55] codes at the PBE/PAW level ("Na_pv" and "Ca_pv" pseudopotentials (PPs) are applied).

n_{Al}	Ca			Na		
	B	M	L	B[a)]	M	L
0	0.041	0.07	0.10	0.038	0.05	0.10
1	0.040	0.07	0.11	0.021	0.05	0.09
2	0.037	0.06	0.11	0.014	0.04	0.08
3	0.036	0.07	0.10	0.006	0.02	0.08

[a)] for Bader Na charges with "Na" PP.

Table 3
Bader (B), Mulliken (M), and Löwdin (L) type charges (*e*) of the Me = Ca and Na (four NaII and four CaII atoms in $Na_4Ca_4Al_{12}Si_{36}O_{96}$) cations with different number of Al atoms per 6R ring (n_{Al}) calculated with Bader [54] and Lobster [55] codes at the PBE/PAW level ("Na_pv" and "Ca_pv" pseudopotentials (PPs) are applied). The MeII atom closest to CO is noted in bold.

Me	n_{Al}	B[a)]	M[b)]	L[c)]
Na	0	0.87	1.02	0.87
		0.87	1.02	0.87
		0.85	**0.98**	**0.79**
		0.87	1.02	0.87
	1	0.87	1.02	0.87
		0.87	1.01	0.87
		0.85	**0.97**	**0.79**
		0.87	1.01	0.87
	2	0.87	1.00	0.87
		0.86	**0.96**	**0.81**
		0.86	0.99	0.87
		0.86	1.00	0.87
	3	0.86	0.99	0.87
		0.86	**0.96**	**0.81**
		0.86	1.00	0.87
		0.86	0.99	0.87
Ca	0	**1.63**	**1.92**	**1.76**
		1.65	1.98	1.84
		1.65	1.98	1.84
		1.65	1.98	1.84
	1	1.64	1.98	1.86
		1.62	**1.90**	**1.77**
		1.64	1.94	1.85
		1.64	2.00	1.87
	2	1.64	1.93	1.85
		1.62	**1.94**	**1.78**
		1.64	1.93	1.84
		1.64	1.93	1.84
	3	1.64	1.93	1.85
		1.62	**1.93**	**1.78**
		1.64	1.93	1.85
		1.64	1.93	1.85

[a)] for Bader Na charges with "Na" PP.
[b)] 0.92–0.94 *e* for Na cations (non coordinated to CO) with "Na" PP at $n_{Al} = 0$.
[c)] 0.78–0.80 *e* for Na cations (non coordinated to CO) with "Na" PP at $n_{Al} = 0$.

Ca. The ratio of the slopes (Fig. 3) for the lines fitted for NaY (3 points for H_2, CO, CO_2) and CaY (7 points without C_2H_2) yields to a 0.561 value, closer to the Bader evaluations.

3.3. Al distribution in the 6R windows of NaY

The relative populations of the NaII sites in NaY which are first occupied by an adsorbate at small coverage should be taken into account to obtain averaged heat values. The common sense hints in favor of the most stable 6R sites with 3 Al atoms per ring. It should produce a tight binding between Na^+ and the oxygen atoms of the Si–O–Al types. The 6R sites with 2 Al should be less stable and so on. The discussion below helps to evaluate the best stabilization considering the NaY model of

Table 4
Bader, Mulliken, and Löwdin type atomic charges (*e*) of the CaII and NaII cations, q(Na)/q(Ca) ratios (the ratio interval $[(q(Na)/q(Ca))_{min}, (q(Na)/q(Ca))_{max}]$ is determined by the range $[q(Na)_{min}/q(Ca)_{max}, q(Na)_{max}/q(Ca)_{min}]$) in the MeY zeolites as calculated with the Bader [54] and Lobster [55] codes at the PBE/-PAW level. The two bottom rows correspond to the V(Na)/V(Ca) rotational barrier ratio from the cNEB calculation for CO_2 and CO.

Type	Me	Charges	$[(q(Na)/q(Ca))_{min}, (q(Na)/q(Ca))_{max}]$
Bader	Ca	1.628–1.641	0.517–0.525
	Na	0.849–0.854	
Mulliken	Ca	1.93–1.96	0.467–0.477
	Na	0.91–0.93	
Löwdin	Ca	1.80–1.84	0.416–0.433
	Na	0.77–0.78	
V(Na)/V(Ca) for CO_2	–	–	0.525[a)]
V(Na)/V(Ca) for CO	–	–	0.358–0.549[a)]

[a)] According to the rotational barriers V, data from Table 1.

Uytterhoeven et al. [44] wherein the highest stability corresponds to the highly symmetric NaY model (4/0/0/4 in Table 5) with 4NaII sites with 3 Al atoms per 6R and 4NaII sites without Al per 6R, for a total of eight NaII sites per UC (U = −1171.819 eV in Table 5), all 8 sites being occupied by 8 Na. The second 3/1/1/3 model is obtained *via* a Al/Si permutation between the initial 6R(3Al) and 6R(0Al) sites thus creating 6R(2Al) and 6R(1Al), respectively. This T site is exposed to the supercage and belongs to the adjacent sodalite cage. The third Al (U = −1170.931 eV) and fourth Al (U = −1169.956 eV) site atoms are shifted from the 4R windows which are parts of the supercage and D6R fragments. In these cases, the energy drop is even larger. So, arbitrary transfers between T sites diminish the total stability by more than 1 eV per UC irrespective of the place of the Si/Al exchange. The same trend is confirmed at the hybrid DFT level (HISS functional [59,60]) using the same geometries as optimized at the PBE-D3 level (Table 5).

The explanation of the results is probably related to the minor energy gain due to the interaction between Na^+ and the Si–O–Al moiety. The latter O atom indeed possesses a larger atomic charge (in absolute value) *versus* the Si–O–Si one [63,74]. But the stronger Na^+-O interactions does not seem to cover the energy differences due to the exchange between the 6R and 4R sites. So, the apparent Al distribution with the lowest fraction $n_{Al} = 0$ in the 6R ring is not the thermodynamically favorite one for NaY (Table 5). The Si sites in the 6R(0Al) rings belong to the Si(1Al) type, which is observed in the ^{29}Si NMR spectra with usually intensive band around of −100 ppm [75].

The interaction energy ΔU values for H_2 near the NaII sites were calculated with variable number of Al atoms per 6R. One observes a steep decline of ΔU due to a lower electric field and electric field gradient (Eq. (2)) produced by NaII at a larger n_{Al} value. The decrease of

Table 5
Total energy U (eV), relative energies ΔU_0 (eV) = U – U(4/0/0/4) of the four NaY(Si/Al = 3) models with different fractions of 6R(n_{Al}) sites corresponding to $n_{Al} = 3, 2, 1$, and 0 Al atoms per 6R window (for a total quantity of eight 6R sites per UC). The different NaY models are obtained *via* Al/Si exchange between the different T positions; the H_2 – NaY interaction energy ΔU (given in eV and kcal/mol to be compared with the values in Table 6) is calculated at one of the 6R (nAl) sites of the same row. The (4/0/0/4) distribution corresponds to the optimized NaY model from ref. [44]. All the NaY models used for the single point calculations with the hybrid HISS functional [59,60] are optimized at the PBE-D3 level of theory.

6R types	-U	ΔU_0		n_{Al}	ΔU(PBE-D3)	
		PBE-D3	HISS		eV	kcal/mol
4/0/0/4	1171.819	0.000	0.000	0	0.121	2.790
3/1/1/3	1171.544	0.275	0.268	1	0.105	2.421
2/2/1/3	1170.931	0.888	0.925	2	0.098	2.260
2/3/0/3	1169.956	1.863	1.950	3	0.097	2.237

the Na charge with n_{Al} is different according to the chosen charge partition schemes in the case of CO near the NaII/6R site in NaY (from a slight q(Na) charge decrease using the Bader or Mulliken scheme to a slight increase or conservation with the Löwdin one as shown in Table 3). But more importantly for H_2 near NaII/6R, the H–NaII distances grow from 2.64 to 2.65 Å ($n_{Al} = 0$) to 2.74 and 2.77 Å ($n_{Al} = 3$) thus confirming a decline of the electric field gradient. The same reasons lead to a parallel decrease of the rotational barrier for all adsorbates. The barrier decrease with n_{Al} is obtained for CO at two positions near the 6R without Al (filled triangle) and with 3Al (open triangle) in NaY (Fig. 3). As the 6R(0Al) sites occur in the most stable (4/0/0/4) model (Table 5) and as these sites result in the highest interaction energy ΔU, their role is important in the H_2/D_2 separation in NaY. Our obtained difference for H_2 is reasonably smaller, 2.421–2.260 kcal/mol in the right part of Table 5 for NaY(Si/Al = 3), than the one for CO_2, 0.48–0.72 kcal/mol between 6R(2Al) and 6R(1Al) [57] but it is important for the heat of H_2 adsorption. One will discuss the respective heats for H_2/D_2 in the next part including the evaluation of the ZPE terms.

3.4. The importance of the rotational ZPE for H_2 adsorption in NaY

Considering NaY, three advantages should be emphasized regarding the analysis of the rotational effects for the heat of adsorption. First, the heat of H_2 adsorption in NaY is approximately in the narrow range of 1.505 [76], 1.600 [77], and 1.648 kcal/mol [78] at small coverages and 2.05 kcal/mol extrapolated at zero H_2 coverage in NaX with a similar [79] or higher [77,80] activity of NaX for the H_2/D_2 separation relative to NaY. Second, a difference in the heats of adsorption between D_2 and H_2 was measured and confirmed as an equilibrium value in coherence with thermodynamic methods [79] so that our approach (without quantum tunneling and any kinetic effects) is justified. Third, the cation distribution in NaY is rather simple ($V_1 \sim 0$) compared to NaX or NaA for which the geometry of the nearest NaIII cations could result in more complex rotational models with other rotational quantum numbers [28,29]. NaII can occupy the 6R window with different Al numbers ($n_{Al} = 0$ - 3) but we consider only the case without Al ($n_{Al} = 0$) as explained in the previous Part 3.3. It was selected in the present work because of the emphasized H_2 - Na interaction compared to other 6R sites with n_{Al} = 1–3. The NaII/6R($n_{Al} = 0$) site thus corresponds to the Henry region wherein the calculated data can be compared to the experimental difference (0.179 kcal/mol) in the heats of adsorption between D_2 and H_2 (or extrapolated to 0.35 kcal/mol from differential heats at zero coverage of NaX) [79]. An analogous value of 0.175 kcal/mol was measured for NaX [81].

The results of the computations are given in Table 6. The potential curves of the center-of-mass vibration *versus* Na cation were calculated with VASP (Fig. 4) and were used to find the part of vibration-rotational ΔZPE_{vr} term ($\Delta ZPE_{vr} = E_{va} + E_{va}$ - E_{rg}, $E_{rg} = 0$ or $2B_{X2}$, for p-H_2/o-D_2 or o-D_2/p-H_2, respectively, in Table 6). For simplicity, the heat of D_2 adsorption at NaII/6R ($n_{Al} = 0$) site was calculated with the same potential energy surface describing the H_2 - NaY interaction. The heats of both ortho- or para-H_2 adsorption at PBE level, 0.922 or 0.800 kcal/mol, respectively (Table 6), are too low compared to the experimental value for NaX zeolite, *i.e.*, 2.400 and 2.050 kcal/mol for D_2 and H_2, at zero coverage [79]. The adsorption heats calculated at the PBE-D3 level, 2.027 and 1.903 kcal/mol for o-H_2 and p-H_2 (Table 6), are closer to the experimental H_2 values at zero NaX coverage due to the dispersive D3 corrections [79]. At this PBE-D3 level, the computations of ZPE were performed for D_2 as well (Table 6) to be compared with the experimental difference of 0.179 kcal/mol between the heats of adsorption of D_2 and H_2 [79]. Despite different absolute values between experiment [79,81], the consequences of the experimental $Q_{ads}(D_2)$ - $Q_{ads}(H_2)$ heat differences for NaA, NaCaA, and NaX obey to a similar order, *i.e.*, 0.211,

Table 7
Contractions of the three shortest Me-O_z bonds ($R_{Me\text{-}Oz}$, Å) between the initial state (IS, the Me cation is weakly attached to the framework oxygens O_z) and transition state (TS, the Me cation is strongly attached to O_z) at the MeII site of the supercage MeY without Al atoms per 6R ring ($n_{Al} = 0$) calculated at the PBE/PAW level. The T-types (the vector directed from Me to the molecular center-of-mass is perpendicular to the molecular axis) and L-types (Me is located along the molecular axis) depend on the quadrupole's sign (S), with the exception of $^3O_2$.

Me	XY	S	State	Type	$R_{Me\text{-}Oz}$
Na	H_2	+	IS	T	2.374, 2.373, 2.377
			TS	L	2.372, 2.373, 2.373
	CO	–	IS	L	2.374, 2.377, 2.382
			TS	T	2.366, 2.367, 2.371
	CO_2	–	IS	L	2.367, 2.368, 2.371
			TS	T	2.355, 2.355, 2.359
Ca	$^3O_2$	–	IS	T	2.374, 2.373, 2.377
			TS	L	2.372, 2.373, 2.373
	CO	–	IS	L	2.379, 2.421, 2.425
			TS	T	2.373, 2.417, 2.418
	N_2O	–	IS	L	2.388, 2.434, 2.438
			TS	T	2.361, 2.402, 2.402
	CO_2	–	IS	L	2.384, 2.432, 2.432
			TS	T	2.364, 2.407, 2.408
	C_2H_2	+	IS	T	2.395, 2.431, 2.441
			TS	L	2.365, 2.405, 2.417

Table 6
Total interaction energy ΔU (kcal/mol) calculated at the PBE and PBE-D3 levels, energies of the lowest center-of-mass vibrational E_{va} (cm^{-1}) and rotational E_{ra} (cm^{-1}) states for adsorbed ortho- and para-X_2 (X = H or D), shift of vibrational and rotational zero-point energies ΔZPE_{vr} (kcal/mol) = $E_{va} + E_{ra}$ - E_{rg} upon adsorption, wherein $E_{rg} = 0$ or $2B_{X2}$, for p-H_2/o-D_2 or o-D_2/p-H_2, respectively, in the gas state (E_{va} is calculated with the LEVEL code, and E_{ra} is calculated from the rotational eigen-problem V (in units of rotational constants B_{X2}) from potential (Eq. (1))), and heats of the adsorption Q_{ads} (kcal/mol) = ΔU – ΔZPE_{vr}, at the NaII site of NaY (B_{H2} of H_2 are 60.62, 60.58 cm^{-1} at the PBE and PBE-D3 levels, respectively). The additional ΔZPE_i contribution (Eq. (4)) to the total ΔZPE (Eq. 5a-b) is given in the text (1 kcal/mol = 349.76 cm^{-1}).

Case	ΔU	E_{va}	X_2	V/B_{X2}	E_{ra}	ΔZPE_{vr} cm^{-1}	ΔZPE_{vr} kcal/mol	Q_{ads}
PBE	1.587	120.4	p	11.58	154.8	275.2	0.787	0.800
			o		233.5	232.6	0.665	0.922
PBE-D3	2.760	137.1	p	12.45	162.6	299.7	0.857	1.903
			o		240.4	256.3	0.733	2.027
PBE-D3[a)]	2.760	99.3	o	24.90	126.8	226.1	0.646	2.114
			p		161.9	200.6	0.574	2.186
Exper.[b)]	–	–	–	–	–	–	–	2.050[c)], 2.400[a,c)], 1.505[d)], 1.600[e)], 1.648[f)]

[a)] D_2.
[b)] for H_2 if no other remark.
[c)] [79].
[d)] [76].
[e)] [77].
[f)] [78].

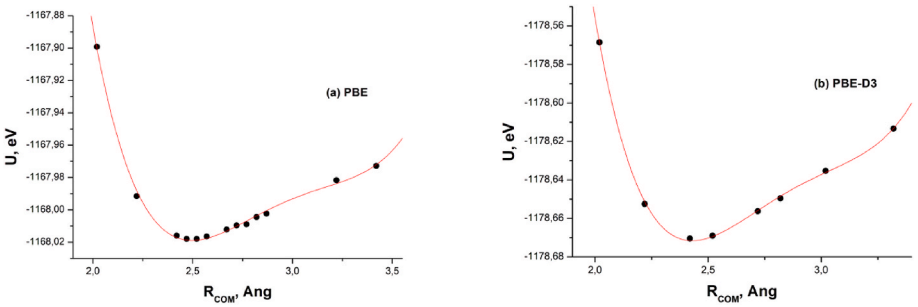

Fig. 4. Potential curves (eV) *versus* the H_2 center-of-mass (COM) - NaII distance (Å) cation obtained at the (a) PBE or (b) PBE-D3 levels and used as input for the LEVEL code [64]. Calculated values (circles) are approximated by a 4th-order polynomial (solid line).

0.135, 0.148 kcal/mol [79] or 0.300, 0.150, 0.175 kcal/mol [81]. Both series were obtained at low temperatures (62.0, 77.3, and 90.4K [79] and 75 and 90K [81]). To be precise, let us to note that the ortho-para content should also be taken into account. The equilibrium (denoted as e−) ratio of 3/1 for ortho-H_2/para-H_2 and the ratio of ½ for para--D_2/ortho-D_2 give:

$$Q_{ads}(e\text{-}D_2) = 0.333 \times Q_{ads}(p\text{-}D_2) + 0.667 \times Q_{ads}(o\text{-}D_2) = 2.138 \text{ kcal/mol} \quad (3a)$$

$$Q_{ads}(e\text{-}H_2) = 0.25 \times Q_{ads}(p\text{-}H_2) + 0.75 \times Q_{ads}(o\text{-}H_2) = 1.996 \text{ kcal/mol} \quad (3b)$$

and a heat difference of 2.138–1.996 = 0.142 kcal/mol that is smaller compared to 0.179 kcal/mol for NaY [29]. If one admits an ortho-para conversion of equilibrium H_2 content (3/1) to normal-H_2 one (1/1) at low temperatures of 77–90 K:

$$Q_{ads}(n\text{-}H_2) = 0.5 \times Q_{ads}(p\text{-}H_2) + 0.5 \times Q_{ads}(o\text{-}H_2) = 1.965 \text{ kcal/mol} \quad (3c)$$

leading to a higher difference of 2.138–1.965 = 0.173 kcal/mol for NaY. A minor increase of the $Q_{ads}(D_2)$ - $Q_{ads}(H_2)$ heat difference (due to a decrease of total ΔZPE) can be evaluated from intramolecular H–H/D-D vibrations on the basis of the experimental IR spectra of H_2/D_2 in the Na_4Ca_4A zeolite [3]. In this zeolite, H_2 shows a very similar behavior compared to NaY regarding the large V barrier (Table 1) and a nearly free rotation parallel to the 6R ring (barrier $V_1 \sim 0$ in Eq. (1)). The IR data relate probably to an H_2/D_2 location at the most occupied CaI site in Na_4Ca_4A (similar to CaII one in NaCaY) so that they can serve as upper boundary for the intramolecular vibrational ΔZPE_i at NaII site. The intramolecular 0 → 1 vibrations of H_2/D_2 in Na_4Ca_4A are red shifted by $\Delta\omega_{ag}(X_2) = -73 \pm 2/-55 \pm 1$ cm^{-1} [3], respectively. A decrease of ΔZPE_i between H_2 and D_2 can then be evaluated using an harmonic approximation (HA) as the difference:

$$\Delta ZPE_i = ½ \times [hc(\Delta\omega_{ag}(D_2) - (\Delta\omega_{ag}(H_2))] = (-55 + 73)/2 = 9 \text{ cm}^{-1} \text{ or } 0.026 \text{ kcal/mol} \quad (4)$$

Summing this correction, one has:

$$\Delta ZPE = \Delta ZPE_{vr} + \Delta ZPE_i = 0.173 + 0.026 = 0.199 \text{ kcal/mol} \quad (5a)$$

for e-D_2/e-H_2 mixture or:

$$\Delta ZPE = \Delta ZPE_{vr} + \Delta ZPE_i = 0.142 + 0.026 = 0.168 \text{ kcal/mol} \quad (5b)$$

for e-D_2/n-H_2 mixture, both close to the experimental $Q_{ads}(D_2)$ - $Q_{ads}(H_2)$ heat differences given above [79,81]. However, the estimations (Eq. 5a-b) should be considered as upper boundaries because the red shift in NaY is smaller (in absolute value) being between $\Delta\omega_{ag}(H_2) = -36$ cm^{-1} [82] and −39, −46 cm^{-1} [83] (no value is known for D_2). The ΔZPE_i term at the NaII site is hence smaller, even if the respective $\Delta\omega_{ag}(D_2)$ value at NaY is unknown. Despite this, the final ΔZPE value (smaller than with Eq. (5a-b)) leads to a good coincidence with the experimental heat difference [79,81] and hence provides a way to an accurate computation of the isotopic separation factors. Surprisingly, the ΔZPE_{vr} estimations for NaY fit properly with the recent data on isosteric ΔH_{st} heats within the range 77–87 K in Cu-based MOF with the **CHA** topology [84]. The ΔH_{st} difference decreases approximately from 0.18 to 0.15 kcal/mol while the D_2/H_2 coverage grows from 0 to ~6 mmol/g (the estimation of 0.15 kcal/mol is from Fig. 5a of ref. [84]). The authors of ref. [84] observed a better D_2/H_2 separation than in NaCaA that indeed corresponds to higher ΔZPE_{vr} values (nearly coinciding herein with the ΔH_{st} difference for FJI-Y11 type) than the experimental data of 0.135 kcal/mol [79] or 0.150 kcal/mol [81] for NaCaA at similar conditions.

3.5. *Out-of-plain and in-plain H_2 rotation*

In the present work, we implemented a scheme to evaluate the rotational barrier V (Eq. (1)) of H_2 in the NaY and NaCaY zeolite using the cNEB method. The knowledge of such rotational barrier is of prime importance for accurate calculations of the adsorption energies of light adsorbates, as H_2 and D_2, since the rotational ZPE could be the essential part of the total ZPE together with the vibrational center-of-mass mode (as compared to the small ΔZPE_i (Eq. (4)) of the intramolecular vibration). At a non-zero barrier, the rotational ZPE for ortho- and para-H_2 (para- and ortho-D_2) increases relative to $2B_{X2}$ and 0 (X = H or D), respectively, for a free X_2 rotor, B_{X2} being the rotational constant. One should note that a lower rotational ZPE determines a slightly higher heat of adsorption (and a better adsorption) for "rotating" ortho-H_2 (at both PBE or PBE-D3 levels) and para-D_2 isotopomers (Table 6) in agreement with chromatographic data for NaA and with the conclusions about the paramount importance of hindered rotations for H_2 adsorption [27]. In terms of a two-dimensional rotor model (Eq. (1)) [65,85] the V barrier corresponds to an out-of-plain rotational barrier λ (using the notations of refs. [28,29,65]). In general, an in-plain rotational barrier μ (parallel to the 6R plane, denoted as V_1 herein) is usually around zero for both NaII and CaII sites [28] (named as NaI and CaI in NaCaA) and hence was not calculated herein. It signifies that adopting a one-dimensional hindered rotor model (out-of-plain) for H_2 based on computations of energies for the lowest rotational levels [85] provides a realistic rotational ZPE energy.

3.6. *Anharmonic character of the potential energy surface*

The treatment of the center-of-mass motions and molecular rotation within the harmonic approximation (HA) is often admitted while the anharmonic (AH) character of the potential energy surface is extremely important for the entropy and free energy [86,87]. The AH character was taken into account for both vibrational and rotational degrees of freedom and leads to a good agreement with the experimental $Q_{ads}(D_2)$ - $Q_{ads}(H_2)$ heat differences at low temperatures [79,81] in absence of rotational - vibrational coupling. This justifies the extrapolation towards the obtained models for higher temperatures for which the AH behavior is of higher importance. Let us note that it is difficult to discuss on a quantitative agreement without any data about ortho-para-H_2/D_2 content at experimental conditions. Due to the high rotational constant of

H_2, the difference between AH and HA models is crucial for the partition functions and the energies of rotational states. The anharmonic character of the potential energy for the center-of-mass motion relative to the cation (the "wall" of the supercage, Fig. 4) made us to apply the LEVEL code because the VASP code calculates harmonic frequencies. The latter cannot provide an accurate ZPE contribution because of the overestimated energy of the ground vibrational state.

3.7. Quantum sieving versus kinetic sieving effects for H_2/D_2

We wish to point out that the large pore diameter in NaY allows the H_2/D_2 molecules to freely pass through the wide 12R windows. Therefore, the absence of kinetic effects can be justified. An earlier similar approach was applied for the calculation of the o-p-H_2 and p-o-D_2 separation coefficients in the narrow pore of $Na_{12}A$ and Na_4Ca_4A [28]. Their adsorption *via* narrower pores (4–5 Å) in the **LTA** types at low temperatures and low (135–160K [27]) or middle (55–110K [28]) X_2 coverages can involve both tunneling and kinetic effects but a reasonable agreement was nevertheless achieved. A slightly worse agreement for H_2 compared to two independent sources of measured o-p-H_2 separation coefficients was indeed observed below 77K [28] but it can be due just by more than 8 molecules per α-cage allowed by the model. The main difference between the current study and ref. [28] is the way to calculate the adsorption energy. In ref. [28], empirical pair-wise potentials with parameters fitted to satisfy IR shifts of adsorbed H_2 were used to describe the eight adsorption sites (positioned at the corners of a distorted cube) in terms of the heterogeneous Ising model with two types of H_2/D_2 adsorption sites (2 + 6 in $Na_{12}A$ and 4 + 4 in Na_4Ca_4A). The current work and refs. [28,29], however, show the main role of the enthalpy factors for the interpretation of H_2/D_2 spin and isotopic separation. At this point, we agree with the opinion that the chemical affinity quantum sieving due to different ZPE and contributions to the partition functions at various centers is a decisive factor for isotope separation in MOFs while kinetic quantum sieving could happen in relatively few systems [32,33].

3.8. A posteriori justification of the approach to estimate the rotational barrier

The cNEB calculations implemented here indicate the complex nature of rotation of the adsorbate and hence cast doubt on the simplified estimations of their rotational barrier in the adsorbent framework. We observe a shift of the cation from its site (relative to the atoms of the nearest 6R ring) along the rotation (the initial and transition states in Table 7). The comparison between the Me-XY initial state geometries (*i.e.*, T-type for positive quadrupoles and L-type for the negative ones) and the transition state (*i.e.*, top of the barrier with opposite molecular L and T-configurations relative to the initial ones) showed a shift of the cation expressed *via* the variation of the $R_{Me\text{-}Oz}$ distance (Table 7). The length of the displacement depends on the adsorbed molecule. It reveals the first additional problem for alternative methods to evaluate the barrier from two different orientations of the molecule (as mentioned in the Introduction). The displacement of the Ca^{2+} cation around its equilibrium position during, for example, the rotation of C_2H_2, *i.e.,* at the minimum, leads to Ca-O_z bonds of 2.395, 2.431, and 2.441 Å *versus* 2.365, 2.405, and 2.417 Å at the transition state when Ca is strongly attached to the framework oxygens (Table 7). Such behavior is also typical for other molecules (Table 7) with a minimal Me shift for H_2 and O_2, with minor variations around some thousandths of Å (possibly at the level of the accuracy of the method used herein).

The second problem with a simplified approach for calculating the barrier in the case of XY = C_2H_2 (positive quadrupole) and N_2O (negative quadrupole) is the deviation of the Ca-XY geometry at the transition state of the rotational profile from the strict L- or T-orientations, respectively (Fig. 2e and h). We assign the angular fluctuations to a specific combination of the electrostatic and dispersive energies. These deviations are however not evident *a priori* and require a direct computation.

3.9. Absence of specifically strong CO_2 interactions with the framework cations

The concept of specific ion - CO_2 quadrupole interactions is often considered to apprehend gas separation effects for CO_2 mixtures. The cationic drift along the rotation (Part 3.8) can serve as a measure of the possible influence of the adsorbed molecule on the cationic position *via* a variation of Me-O_z distance upon rotation. For CO_2, one notes no stronger interaction between both Na and Ca cations compared to the other adsorbed molecules. The Me-O_z shortening is 0.01 Å upon either CO_2 or CO drift to the top of the barrier along the trajectory in NaY (Table 7). A higher variation of ~0.03 Å of the Ca-O_z bonds in CaY is obtained for C_2H_2 and N_2O rotations compared to the one for CO_2, ~0.02 Å. In CaY, the order of the shifts corresponds to the sequence: O_2 < CO < CO_2 < C_2H_2 < N_2O (Table 7). It also signifies that no specific and stronger CO_2 interaction with Na or Ca located in 6R windows was observed relative to the ones with other adsorbates, as periodically questioned in literature mainly regarding 8R positions [26].

4. Conclusions

Rotational barriers for eight molecules, H_2, N_2, O_2, CO, CO_2, NO, N_2O, and C_2H_2, were calculated at the MeII sites in the NaY and NaCaY zeolites using periodic DFT, the cNEB method, and VASP code. Additional efforts were addressed to the molecules with a positive quadrupole (H_2, C_2H_2) and $^3O_2$ while applying cNEB because of the obtained equilibrium T-geometry *versus* the cation. Such approach for a molecule with positive quadrupole near a cation realized above can be also addressed to a molecule with negative quadrupole close to the anion (for example, a framework O atom) when a T-geometry has also been obtained. As H_2 possesses rather high vibrational and rotational ZPE values, the latter have to be calculated when adsorbed in zeolites, or in MOFs. The rotational ZPE can be estimated with the approach of Sams and Mac-Rury admitting the decoupling of the vibrational motion of the center of mass and the rotational motion of the H_2 axis. Both barriers are required for the method of Sams and Mac-Rury but cNEB can determine the lowest barrier for the H_2 rotation parallel to an approximate 6R plane. As initial guess for the profile along the θ-rotation (the highest barrier), a combination of two initial profiles for cNEB both containing a common intermediate state near the top of the barrier was proposed. This led to a qualitative agreement with experimental $Q_{ads}(D_2)$ - $Q_{ads}(H_2)$ heat differences. An essential fraction of the NaII/6R sites without Al in the 6R window was shown to be the consequence of the most stable NaY model that had been earlier derived by Uytterhoeven et al. Analogous relative stabilities of the NaY models with different Al distributions in 6R were obtained at the GGA (PBE-D3) and hybrid (HISS) functionals. A further step for a quantitative agreement could only be discussed on the basis of data with a known ortho-para-H_2/D_2 content at the experimental conditions which are yet absent to our best knowledge. Analogous sites in the 6R windows are extremely frequent for a wide set of the sieves as **AEI, ERI, FAU, GME, KFI, LEV, LTA, LTL, LTN, MWW, OFF**, *etc*. The important issue is that the quadrupole – gradient field interaction dominates throughout the series of eight molecules in the rotational barrier, while dipole terms hinders weakly the rotation of CO, NO, and N_2O. Traditionally, most authors addressed to the lowest permanent electric moment, like CO dipole, while discussing its diffusion. Regarding the choice of the effective atomic charges in empirical potentials for the CO, NO, and N_2O adsorption, one strongly insists on the primary importance of the quadrupole fitting compared to the relatively small dipole values. The addition of atomic charges in empirical potentials to simulate the molecular quadrupole values helps to avoid the rotation of the adsorbed molecules with a non-zero quadrupole but is not able to properly involve the important

rotational correlation along the diffusion.

CRediT authorship contribution statement

A.A. Rybakov: Visualization, Writing – review & editing, Investigation, Software, Methodology. **D.N. Trubnikov:** Funding acquisition, Writing – review & editing. **D.P. Vercauteren:** Resources, Supervision, Writing – review & editing, Conceptualization. **A.V. Larin:** Writing – original draft, Investigation, Conceptualization.

Declaration of competing interest

The authors declare that they have no known competing financial interests or personal relationships that could have appeared to influence the work reported in this paper.

Data availability

Data will be made available on request.

Acknowledgements

The authors thank the Russian Foundation of Basic Research within the grant 20-53-18001 Bolg_a. The research has been carried out using the equipment of the shared research facilities of HPC computing resources at Lomonosov Moscow State University [88].

The authors also acknowledge the Plateforme Technologique de Calcul Intensif (P.T.C.I.; http://www.ptci.unamur.be), located at the University of Namur, which is part of the Consortium des Equipements de Calcul Intensif (C.E.C.I., supported by the F.R.S.-FNRS, Belgium; http://www.ceci-hpc.be).

Appendix A. Supplementary data

Supplementary data to this article can be found online at https://doi.org/10.1016/j.matchemphys.2022.126929.

References

[1] J.A. Michelena, G. Peeters, E.F. Vansant, P. de Bièvre, Recueil des Travaux Chimiques des Pays-Bas Journal of the Royal Netherlands Chemical Society: the adsorption of carbon monoxide and carbon dioxide in calcium-exchanged zeolite Y, Recl. Trav. Chim. Pays-Bas 96 (1977) 121–124, https://doi.org/10.1002/recl.19770960502.

[2] E. Cohen de Lara, Y. Delaval, Infrared spectra of nitrogen adsorbed in NaA zeolite. Experimental determination of electrostatic field in the cavities from induced band intensity and comparison with theoretical results, J. Chem. Soc., Faraday Trans. 2 (74) (1978) 790–797, https://doi.org/10.1039/f29787400790.

[3] H. Förster, M. Schuldt, Molecular motion studies of A_2 molecules encaged in zeolites, J. Mol. Struct. 47 (1978) 339–343, https://doi.org/10.1016/0022-2860(78)87200-7.

[4] K. Hadjiivanov, H. Knözinger, E. Ivanova, L. Dimitrov, FTIR study of low-temperature CO and $^{15}N_2$ adsorption on a CaNaY zeolite: formation of site-specified $Ca^{2+}(CO)_3$ and $Ca^{2+}(^{15}N_2)_3$ complexes, Phys. Chem. Chem. Phys. 3 (2001) 2531–2536, https://doi.org/10.1039/b101782i.

[5] E.A. Paukshtis, R.I. Soltanov, E.N. Yurchenko, IR spectroscopic studies of low-temperature CO adsorption on CaNaY zeolite, React. Kinet. Catal. Lett. 22 (1983) 147–151, https://doi.org/10.1007/BF02064823.

[6] A.A. Tsyganenko, Lateral interactions between adsorbed molecules, in: Aspects of the Surface Chemistry of Oxidic Systems, Edizioni Libreria Cortina, Turin, 1999, pp. 51–57.

[7] A.A. Tsyganenko, E. Escalona Platero, C. Otero Areán, E. Garrone, A. Zecchina, Variable-temperature IR spectroscopic studies of CO adsorbed on Na-ZSM-5 and Na-Y zeolites, Catal. Lett. 61 (1999) 187–192, https://doi.org/10.1023/A:1019089309446.

[8] K. Hadjiivanov, H. Knözinger, Formation of $Ca^{2+}(CO)_3$ complexes during low-temperature CO adsorption on CaNaY zeolite, J. Phys. Chem. B 105 (2001) 4531–4534, https://doi.org/10.1021/jp004248m.

[9] E. Garrone, B. Bonelli, A.A. Tsyganenko, M. Rodríguez Delgado, G. Turnes Palomino, O.V. Manoilova, C. Otero Areán, Spectroscopic and thermodynamic characterization of strontium carbonyls formed upon carbon monoxide adsorption on the zeolite Sr−Y, J. Phys. Chem. B 107 (2003) 2537–2542, https://doi.org/10.1021/jp0217841.

[10] B. Bonelli, C. Otero Areán, M. Armandi, M.R. Delgado, E. Garrone, Variable-temperature infrared spectroscopy studies on the thermodynamics of CO adsorption on the zeolite Ca-Y, ChemPhysChem 9 (2008) 1747–1751, https://doi.org/10.1002/cphc.200800238.

[11] J. Soussen-Jacob, J. Tsakiris, E. Cohen de Lara, Adsorption of oxygen molecule in NaA zeolite: isotherms and infrared measurements, J. Chem. Phys. 91 (1989) 2649–2655, https://doi.org/10.1063/1.456974.

[12] F. Jousse, E. Cohen de Lara, Induced infrared absorption of molecular oxygen sorbed in exchanged A zeolites. 1. Intensity analysis, J. Phys. Chem. 100 (1996) 233–237, https://doi.org/10.1021/jp951144g.

[13] F. Stéphanie-Victoire, E. Cohen de Lara, Adsorption and coadsorption of molecular hydrogen isotopes in zeolites. II. Infrared analyses of H_2, HD, and D_2 in NaA, J. Chem. Phys. 109 (1998) 6469–6475, https://doi.org/10.1063/1.477292.

[14] J.G. Vitillo, L. Regli, S. Chavan, G. Ricchiardi, G. Spoto, P.D.C. Dietzel, S. Bordiga, A. Zecchina, Role of exposed metal sites in hydrogen storage in MOFs, J. Am. Chem. Soc. 130 (2008) 8386–8396, https://doi.org/10.1021/ja8007159.

[15] S.A. FitzGerald, K. Allen, P. Landerman, J. Hopkins, J. Matters, R. Myers, J.L. C. Rowsell, Quantum dynamics of adsorbed H_2 in the microporous framework MOF-5 analyzed using diffuse reflectance infrared spectroscopy, Phys. Rev. B 77 (2008), 224301, https://doi.org/10.1103/PhysRevB.77.224301.

[16] S.A. FitzGerald, J. Hopkins, B. Burkholder, M. Friedman, J.L.C. Rowsell, Quantum dynamics of adsorbed normal- and para-H_2, HD, and D_2 in the microporous framework MOF-74 analyzed using infrared spectroscopy, Phys. Rev. B 81 (2010), 104305, https://doi.org/10.1103/PhysRevB.81.104305.

[17] T. Pham, K.A. Forrest, A. Hogan, K. McLaughlin, J.L. Belof, J. Eckert, B. Space, Simulations of hydrogen sorption in rht-MOF-1: identifying the binding sites through explicit polarization and quantum rotation calculations, J. Mater. Chem. A. 2 (2014) 2088–2100, https://doi.org/10.1039/C3TA14591C.

[18] T. Pham, K.A. Forrest, P.A. Georgiev, W. Lohstroh, D.-X. Xue, A. Hogan, M. Eddaoudi, B. Space, J. Eckert, A high rotational barrier for physisorbed hydrogen in an fcu-metal–organic framework, Chem. Commun. 50 (2014) 14109–14112, https://doi.org/10.1039/C4CC05987E.

[19] T. Pham, K.A. Forrest, E.H.L. Falcão, J. Eckert, B. Space, Exceptional H_2 sorption characteristics in a Mg^{2+} -based metal–organic framework with small pores: insights from experimental and theoretical studies, Phys. Chem. Chem. Phys. 18 (2016) 1786–1796, https://doi.org/10.1039/C5CP05906B.

[20] S. Suepaul, K.A. Forrest, P.A. Georgiev, P.M. Forster, W. Lohstroh, V. Grzimek, S. G. Dunning, J.E. Reynolds, S.M. Humphrey, J. Eckert, B. Space, T. Pham, Investigating H_2 adsorption in isostructural metal–organic frameworks M-CUK-1 (M = Co and Mg) through experimental and theoretical studies, ACS Appl. Mater. Interfaces 14 (2022) 8126–8136, https://doi.org/10.1021/acsami.1c20312.

[21] A.A. Rybakov, A.V. Larin, D.P. Vercauteren, CO diffusion as a re-orientation mechanism in the NaY zeolite, Phys. Chem. Chem. Phys. 19 (2017), 20930, https://doi.org/10.1039/C7CP03043F. –20940.

[22] G.L. Kington, A.C. Macleod, Heats of sorption of gases in chabazite, energetic heterogeneity and the role of quadrupoles in sorption, Trans. Faraday Soc. 55 (1959) 1799–1804, https://doi.org/10.1039/tf9595501799.

[23] D. Newsome, M.-O. Coppens, Molecular dynamics as a tool to study heterogeneity in zeolites – effect of Na^+ cations on diffusion of CO_2 and N_2 in Na-ZSM-5, Chem. Eng. Sci. 121 (2015) 300–312, https://doi.org/10.1016/j.ces.2014.09.024.

[24] A.V. Larin, A. Mace, A.A. Rybakov, A. Laaksonen, Carbonate “door” in the NaKA zeolite as the reason of higher CO_2 uptake relative to N_2, Microporous Mesoporous Mater. 162 (2012) 98–104, https://doi.org/10.1016/j.micromeso.2012.06.005.

[25] G.K. Li, J. Shang, Q. Gu, R.V. Awati, N. Jensen, A. Grant, X. Zhang, D.S. Sholl, J. Z. Liu, P.A. Webley, E.F. May, Temperature-regulated guest admission and release in microporous materials, Nat. Commun. 8 (2017), 15777, https://doi.org/10.1038/ncomms15777.

[26] I.A. Bryukhanov, A.A. Rybakov, A.V. Larin, Carbonate-promoted drift of alkali cations in small pore zeolites: ab Initio molecular dynamics study of CO_2 in NaKA zeolite, J. Phys. Chem. Lett. 10 (2019) 2191–2195, https://doi.org/10.1021/acs.jpclett.9b00519.

[27] P.L. Gant, K. Yang, M.S. Goldstein, M.P. Freeman, A.I. Weiss, Role of hindered rotation in the physical adsorption of hydrogen weight and spin isomers, J. Phys. Chem. 74 (1970) 1985–1991, https://doi.org/10.1021/j100704a028.

[28] A.V. Larin, V.S. Parbuzin, Theoretical estimate of ortho-para separation coefficients for H_2 and D_2 on A-type zeolites for small and medium coverage, Mol. Phys. 77 (1992) 869–891, https://doi.org/10.1080/00268979200102841.

[29] A.V. Larin, E. Cohen de Lara, Estimate of ionicity of zeolite NaA using the frequency shift values of physisorbed molecular hydrogen, Mol. Phys. 88 (1996) 1399–1410, https://doi.org/10.1080/00268979650025911.

[30] F.M. Mulder, T.J. Dingemans, H.G. Schimmel, A.J. Ramirez-Cuesta, G.J. Kearley, Hydrogen adsorption strength and sites in the metal organic framework MOF5: comparing experiment and model calculations, Chem. Phys. 351 (2008) 72–76, https://doi.org/10.1016/j.chemphys.2008.03.034.

[31] L. Kong, G. Román-Pérez, J.M. Soler, D.C. Langreth, Energetics and dynamics of H_2 adsorbed in a nanoporous material at low temperature, Phys. Rev. Lett. 103 (2009), 096103, https://doi.org/10.1103/PhysRevLett.103.096103.

[32] H. Oh, I. Savchenko, A. Mavrandonakis, T. Heine, M. Hirscher, Highly effective hydrogen isotope separation in nanoporous metal–organic frameworks with open metal sites: direct measurement and theoretical analysis, ACS Nano 8 (2014) 761–770, https://doi.org/10.1021/nn405420t.

[33] I. Savchenko, A. Mavrandonakis, T. Heine, H. Oh, J. Teufel, M. Hirscher, Hydrogen isotope separation in metal-organic frameworks: kinetic or chemical affinity quantum-sieving? Microporous Mesoporous Mater. 216 (2015) 133–137, https://doi.org/10.1016/j.micromeso.2015.03.017.

[34] J.Y. Kim, J. Park, J. Ha, M. Jung, D. Wallacher, A. Franz, R. Balderas-Xicohténcatl, M. Hirscher, S.G. Kang, J.T. Park, I.H. Oh, H.R. Moon, H. Oh, Specific isotope-responsive breathing transition in flexible metal–organic frameworks, J. Am. Chem. Soc. 142 (2020) 13278–13282, https://doi.org/10.1021/jacs.0c04277.

[35] Z. Ju, E.-S.M. El-Sayed, D. Yuan, Dynamic metal–organic frameworks for the separation of hydrogen isotopes, Dalton Trans. 49 (2020) 16617–16622, https://doi.org/10.1039/D0DT02806A.

[36] A.V. Larin, F. Jousse, L. Leherte, D.P. Vercauteren, Theoretical estimation of the vibrational perturbation of the molecular properties of hydrogen adsorbed within a zeolite A framework, Chem. Phys. Lett. 274 (1997) 345–353, https://doi.org/10.1016/S0009-2614(97)00682-9.

[37] A.V. Larin, L. Leherte, D.P. Vercauteren, D.N. Trubnikov, Linear dependence of the interaction energy on intramolecular distance for adsorbed or clustered diatomic molecules, Mol. Phys. 98 (2000) 1433–1439, https://doi.org/10.1080/002689700417547.

[38] G. Henkelman, B.P. Uberuaga, H. Jónsson, A climbing image nudged elastic band method for finding saddle points and minimum energy paths, J. Chem. Phys. 113 (2000) 9901–9904, https://doi.org/10.1063/1.1329672.

[39] D. Sheppard, R. Terrell, G. Henkelman, Optimization methods for finding minimum energy paths, J. Chem. Phys. 128 (2008), 134106, https://doi.org/10.1063/1.2841941.

[40] G. Kresse, J. Hafner, Ab initio molecular dynamics for liquid metals, Phys. Rev. B 47 (1993) 558–561, https://doi.org/10.1103/PhysRevB.47.558.

[41] G. Kresse, D. Joubert, From ultrasoft pseudopotentials to the projector augmented-wave method, Phys. Rev. B 59 (1999) 1758–1775, https://doi.org/10.1103/PhysRevB.59.1758.

[42] A.V. Larin, D.P. Vercauteren, C. Lamberti, S. Bordiga, A. Zecchina, Interaction between probe molecules and zeolites. Part II: interpretation of the IR spectra of CO and N_2 adsorbed in NaY and NaRbY, Phys. Chem. Chem. Phys. 4 (2002) 2424–2433, https://doi.org/10.1039/b107242k.

[43] A.V. Larin, L. Leherte, D.P. Vercauteren, Interaction between probe molecules and zeolites. Part I: pair-wise addition scheme applied to the calculation of the interaction energy of CO and N_2 adsorbed in Na_4Ca_4A, Phys. Chem. Chem. Phys. 4 (2002) 2416–2423, https://doi.org/10.1039/b107243a.

[44] L. Uytterhoeven, D. Dompas, W.J. Mortier, Theoretical investigations on the interaction of benzene with faujasite, J. Chem. Soc., Faraday Trans. 88 (1992) 2753–2760, https://doi.org/10.1039/FT9928802753.

[45] J.P. Perdew, K. Burke, M. Ernzerhof, Generalized gradient approximation made simple, Phys. Rev. Lett. 77 (1996) 3865–3868, https://doi.org/10.1103/PhysRevLett.77.3865.

[46] A.V. Terentjev, L.A. Constantin, J.M. Pitarke, Dispersion-corrected PBEsol exchange-correlation functional, Phys. Rev. B 98 (2018), 214108, https://doi.org/10.1103/PhysRevB.98.214108.

[47] P.E. Blöchl, Projector augmented-wave method, Phys. Rev. B 50 (1994), 17953, https://doi.org/10.1103/PhysRevB.50.17953. –17979.

[48] S. Grimme, J. Antony, S. Ehrlich, H. Krieg, A consistent and accurate ab initio parametrization of density functional dispersion correction (DFT-D) for the 94 elements H-Pu, J. Chem. Phys. 132 (2010), 154104, https://doi.org/10.1063/1.3382344.

[49] S. Grimme, S. Ehrlich, L. Goerigk, Effect of the damping function in dispersion corrected density functional theory, J. Comput. Chem. 32 (2011) 1456–1465, https://doi.org/10.1002/jcc.21759.

[50] E. Caldeweyher, J.-M. Mewes, S. Ehlert, S. Grimme, Extension and evaluation of the D4 London-dispersion model for periodic systems, Phys. Chem. Chem. Phys. 22 (2020) 8499–8512, https://doi.org/10.1039/D0CP00502A.

[51] R.F.W. Bader, Atoms in molecules, Acc. Chem. Res. 18 (1985) 9–15, https://doi.org/10.1021/ar00109a003.

[52] R.S. Mulliken, Electronic population analysis on LCAO–MO molecular wave functions. I, J. Chem. Phys. 23 (1955) 1833–1840, https://doi.org/10.1063/1.1740588.

[53] P. Löwdin, On the non-orthogonality problem connected with the use of atomic wave functions in the theory of molecules and crystals, J. Chem. Phys. 18 (1950) 365–375, https://doi.org/10.1063/1.1747632.

[54] W. Tang, E. Sanville, G. Henkelman, A grid-based Bader analysis algorithm without lattice bias, J. Phys. Condens. Matter 21 (2009), 084204, https://doi.org/10.1088/0953-8984/21/8/084204.

[55] S. Maintz, V.L. Deringer, A.L. Tchougréeff, R. Dronskowski, LOBSTER: a tool to extract chemical bonding from plane-wave based DFT, J. Comput. Chem. 37 (2016) 1030–1035, https://doi.org/10.1002/jcc.24300.

[56] G. Feng, D. Yang, D. Kong, J. Liu, Z.-H. Lu, A comparative computational study on the synthesis prescriptions, structures and acid properties of B-, Al- and G-incorporated MTW-type zeolites, RSC Adv. 4 (2014) 47906–47920, https://doi.org/10.1039/C4RA06114D.

[57] H.V. Thang, L. Grajciar, P. Nachtigall, O. Bludský, C.O. Areán, E. Frýdová, R. Bulánek, Adsorption of CO2 in FAU zeolites: effect of zeolite composition, Catal. Today 227 (2014) 50–56, https://doi.org/10.1016/j.cattod.2013.10.036.

[58] R. Dovesi, A. Erba, R. Orlando, C.M. Zicovich-Wilson, B. Civalleri, L. Maschio, M. Rérat, S. Casassa, J. Baima, S. Salustro, B. Kirtman, Quantum-mechanical Condensed Matter Simulations with CRYSTAL, Wiley Interdiscip Rev Comput Mol Sci., 2018, https://doi.org/10.1002/wcms.1360.

[59] T.M. Henderson, A.F. Izmaylov, G.E. Scuseria, A. Savin, The importance of middle-range Hartree-Fock-type exchange for hybrid density functionals, J. Chem. Phys. 127 (2007), 221103, https://doi.org/10.1063/1.2822021.

[60] T.M. Henderson, A.F. Izmaylov, G.E. Scuseria, A. Savin, Assessment of a middle-range hybrid functional, J. Chem. Theor. Comput. 4 (2008) 1254–1262, https://doi.org/10.1021/ct800149y.

[61] R. Dovesi, C. Roetti, C. Freyria-Fava, M. Prencipe, V.R. Saunders, On the elastic properties of lithium, sodium and potassium oxide. An ab initio study, Chem. Phys. 156 (1991) 11–19, https://doi.org/10.1016/0301-0104(91)87032-Q.

[62] M.F. Peintinger, D.V. Oliveira, T. Bredow, Consistent Gaussian basis sets of triple-zeta valence with polarization quality for solid-state calculations, J. Comput. Chem. 34 (2013) 451–459, https://doi.org/10.1002/jcc.23153.

[63] A.V. Larin, I.K. Sakodynskaya, D.N. Trubnikov, Convergence of electric field and electric field gradient versus atomic basis sets in all-siliceous and Mg substituted phillipsites, J. Comput. Chem. 29 (2008) 2344–2358, https://doi.org/10.1002/jcc.20973.

[64] R.J. le Roy, LEVEL: a computer program for solving the radial Schrödinger equation for bound and quasibound levels, J. Quant. Spectrosc. Radiat. Transf. 186 (2017) 167–178, https://doi.org/10.1016/j.jqsrt.2016.05.028.

[65] T.B. MacRury, J.R. Sams, Hindered rotation of adsorbed diatomic molecules, Mol. Phys. 19 (1970) 337–352, https://doi.org/10.1080/00268977000101351.

[66] A.V. Larin, S.V. Poljanskii, D.N. Trubnikov, Assignment of the torsional structure of the O_0^0 band of the electronic transition $A_{1g} \rightarrow B_{2u}$ in van der Waals clusters of type C_6H_6-X (X = N_2, CO_2, CO), Chem. Phys. Lett. 213 (1993) 619–626, https://doi.org/10.1016/0009-2614(93)89171-D.

[67] P. Ugliengo, D. Viterbo, G. Chiari, MOLDRAW: molecular graphics on a personal computer, Z. für Kristallogr. - Cryst. Mater. 207 (1993) 9–23, https://doi.org/10.1524/zkri.1993.207.12.9.

[68] B.M. Bode, M.S. Gordon, MacMolPlt: a graphical user interface for GAMESS, J. Mol. Graph. Model. 16 (1998) 133–138, https://doi.org/10.1016/S1093-3263(99)00002-9.

[69] W.J. Mortier, J.J. Pluth, J.V. Smith, Positions of cations and molecules in zeolites with the chabazite framework II Adsorption of carbon monoxide on dehydrated Ca-exchanged chabazite, Mater. Res. Bull. 12 (1977) 103–108, https://doi.org/10.1016/0025-5408(77)90095-2.

[70] J.S. Muenter, Electric dipole moment of carbon monoxide, J. Mol. Spectrosc. 55 (1975) 490–491, https://doi.org/10.1016/0022-2852(75)90287-8.

[71] E.L. Uzunova, H. Mikosch, J. Hafner, Adsorption of NO on Cu-SAPO-34 and Co-SAPO-34: a periodic DFT study, J. Phys. Chem. C 112 (2008) 2632–2639, https://doi.org/10.1021/jp0774903.

[72] K. Mogi, T. Komine, K. Hirao, A theoretical study on the dipole moment of N_2O and the weakly bound complexes formed by N_2O, J. Chem. Phys. 95 (1991) 8999–9008, https://doi.org/10.1063/1.461231.

[73] H. Förster, W. Frede, Induced IR overtone and fundamental bands of isotopic H_2 molecules adsorbed in NaCaA zeolites, Infrared Phys. 24 (1984) 151–156, https://doi.org/10.1016/0020-0891(84)90063-0.

[74] A.V. Larin, R.A. Semenyuk, D.N. Trubnikov, D.P. Vercauteren, Electrostatic potential and field approximation for aluminosilicates in cation-substituted forms, Russ. J. Phys. Chem. A 81 (2007) 493–509, https://doi.org/10.1134/S0036024407040012.

[75] D. Freude, J. Klinowski, H. Hamdan, Solid-state NMR studies of the geometry of brønsted acid sites in zeolitic catalysts, Chem. Phys. Lett. 149 (1988) 355–362, https://doi.org/10.1016/0009-2614(88)85107-8.

[76] S.W. Jhung, J.S. Lee, J.W. Yoon, D.P. Kim, J.-S. Chang, Low-temperature adsorption of hydrogen on ion-exchanged Y zeolites, Int. J. Hydrogen Energy 32 (2007) 4233–4237, https://doi.org/10.1016/j.ijhydene.2007.05.014.

[77] M. Kubo, Y. Kamimura, K. Itabashi, T. Okubo, Cryogenic hydrogen adsorption onto H-, Li-, Na-exchanged zeolites with various Si/Al ratios, Adsorpt. Sci. Technol. 32 (2014) 413–423, https://doi.org/10.1260/0263-6174.32.5.413.

[78] S.H. Jhung, J.W. Yoon, J.S. Lee, J.-S. Chang, Low-temperature adsorption/storage of hydrogen on FAU, MFI, and MOR zeolites with various Si/Al ratios: effect of electrostatic fields and pore structures, Chem. Eur J. 13 (2007) 6502–6507, https://doi.org/10.1002/chem.200700148.

[79] V.S. Parbuzin, G.M. Panchenkov, Thermodynamics of hydrogen isotope sorption on synthetic zeolites, Isotopenpraxis Isotopes in Environmental and Health Studies 3 (1967) 56–62, https://doi.org/10.1080/10256016708623005.

[80] M. Giraudet, I. Bezverkhyy, G. Weber, C. Dirand, M. Macaud, J.-P. Bellat, D_2/H_2 adsorption selectivity on FAU zeolites at 77.4 K: Influence of Si/Al ratio and cationic composition, Microporous Mesoporous Mater. 270 (2018) 211–219, https://doi.org/10.1016/j.micromeso.2018.05.026.

[81] D. Basmadjian, Adsorption equilibria of hydrogen, deuterium, and their mixtures. Part I, Can. J. Chem. 38 (1960) 141–148, https://doi.org/10.1139/v60-016.

[82] E.N. Gribov, D. Cocina, G. Spoto, S. Bordiga, G. Ricchiardi, A. Zecchina, Vibrational and thermodynamic properties of Ar, N_2, O_2, H_2 and CO adsorbed and condensed into (H,Na)-Y zeolite cages as studied by variable temperature IR spectroscopy, Phys. Chem. Chem. Phys. 8 (2006) 1186, https://doi.org/10.1039/b513367j.

[83] C. Otero Areán, G. Turnes Palomino, M.R. Llop Carayol, Variable temperature FT-IR studies on hydrogen adsorption on the zeolite (Mg,Na)-Y, Appl. Surf. Sci. 253 (2007) 5701–5704, https://doi.org/10.1016/j.apsusc.2006.12.050.

[84] Y. Si, X. He, J. Jiang, Z. Duan, W. Wang, D. Yuan, Highly effective H_2/D_2 separation in a stable Cu-based metal-organic framework, Nano Res. 14 (2021) 518–525, https://doi.org/10.1007/s12274-019-2571-9.

[85] A.A. Evett, Second-order perturbation calculation of the hindered rotator model for adsorbed hydrogen, J. Chem. Phys. 33 (1960) 789–794, https://doi.org/10.1063/1.1731263.

[86] G. Collinge, S.F. Yuk, M.-T. Nguyen, M.-S. Lee, V.-A. Glezakou, R. Rousseau, Effect of collective dynamics and anharmonicity on entropy in heterogenous catalysis: building the case for advanced molecular simulations, ACS Catal. 10 (2020) 9236–9260, https://doi.org/10.1021/acscatal.0c01501.

[87] J. Amsler, P.N. Plessow, F. Studt, T. Bučko, Anharmonic correction to adsorption free energy from DFT-based MD using thermodynamic integration, J. Chem. Theor. Comput. 17 (2021) 1155–1169, https://doi.org/10.1021/acs.jctc.0c01022.

[88] V.V. Voevodin, A.S. Antonov, D.A. Nikitenko, P.A. Shvets, S.I. Sobolev, I. Yu Sidorov, K.S. Stefanov, VadV. Voevodin, S.A. Zhumatiy, Supercomputer lomonosov-2: large scale, deep monitoring and fine analytics for the user community, Supercomput Front Innov 6 (2019) 4–11. https://superfri.org/superfri/article/view/278.

[89] D.E. Stogryn, A.P. Stogryn, Molecular multipole moments, Mol. Phys. 11 (1966) 371–393, https://doi.org/10.1080/00268976600101201.

[90] J.D. Poll, L. Wolniewicz, The quadrupole moment of the H_2 molecule, J. Chem. Phys. 68 (1978) 3053–3058, https://doi.org/10.1063/1.436171.

[91] C. Graham, J. Pierrus, R.E. Raab, Measurement of the electric quadrupole moments of CO_2, CO and N_2, Mol. Phys. 67 (1989) 939–955, https://doi.org/10.1080/00268978900101551.

[92] D.V.G.L. Narasimha Rao, Molecular quadrupole moment of nitric oxide, Nature 186 (1960) 881–882, https://doi.org/10.1038/186881a0.

[93] N. Chetty, V.W. Couling, Measurement of the electric quadrupole moment of N_2O, J. Chem. Phys. 134 (2011), 144307, https://doi.org/10.1063/1.3578609.

[94] A. Halkier, S. Coriani, On the molecular electric quadrupole moment of C_2H_2, Chem. Phys. Lett. 303 (1999) 408–412, https://doi.org/10.1016/S0009-2614(99)00269-9.